Choi, S., Götze, H.-J., Meyer, U., DESIRE GROUP (2011): 3D density modelling of underground structures and spatial distribution of salt diapirism in the Dead Sea Basin. - Geophysical Journal International, 184, 3, pp. 1131—1146.

DOI: http://doi.org/10.1111/j.1365-246X.2011.04939.x

Geophysical Journal International

Geophys. J. Int. (2011) **184,** 1131–1146 doi: 10.1111/j.1365-246X.2011.04939.x

3-D density modelling of underground structures and spatial distribution of salt diapirism in the Dead Sea Basin

Sungchan Choi,[1] H.-J. Götze,[1] U. Meyer[2] and DESIRE Group[3]

[1] *Institut für Geowissenschaften, Abtlg. Geophysik, Christian-Albrechts-Universität zu Kiel, Otto-Hahn-Platz* 1, 24118 *Kiel, Gemany. E-mail: choi@geophysik.uni-kiel.de*

[2] *Bundesanstalt für Geowissenschaften und Rohstoffe, Geozentrum Hannover, Stilleweg* 2, 30655 *Hannover, Germany*

[3] *GeoForschungsZentrum Potsdam, Telegrafenberg Haus E* 325, 14473 *Potsdam, Germany*

Accepted 2011 January 3. Received 2010 December 15; in original form 2010 August 29

SUMMARY

A new compilation of Bouguer gravity data stemming from airborne, shipborne and terrestrial data set in the entire Dead Sea Basin (DSB) was reinterpreted by applying 3-D density modelling that incorporated independent information on other geophysical researches allowing for regional and residual filtering in the gravity field, carrying out curvature analysis and Euler deconvolution of the combined gravity field. 3-D density modelling enables us to detailed resolution of upper crustal structures from the southern to the northern subbasin below the saline Dead Sea. 3-D gravity modelling led to the identification of three salt structures, which are found beneath the Sedom area, the Lisan Peninsula and the Dead Sea. In the vicinity of the western margin of the Dead Sea, a salt diapir segment with a thickness of about 4 km has been identified at a top depth of about 2 km, which has not been recognised by any other geophysical interpretations. The thickness of the sedimentary infill overlying the basement in the DSB decreases from 14 km in the vicinity of the Lisan Peninsula to 8 km in the northern and the southern subbasins. Large negative gravity anomalies (lower than -100×10^{-5} m s^{-2}) observed in the DSB correspond with the spatial distribution of salt diapirism with an average density of 2 100 kg m^{-3}. The shallower microearthquakes registered in the DSB are related to the movement of salt diapir in the DSB.

Key words: Numerical approximations and analysis; Gravity anomalies and Earth structure; Transform faults; Crustal structure; Diapir and diapirism: Asia.

1 INTRODUCTION

Salt diapirs are widespread phenomena, which occur at continental margins, for example, in the North Sea (Lyngsie *et al.* 2006), the Gulf of Mexico (Rowan *et al.* 1999) and the Zagros mountains (Aftabi *et al.* 2010). Here, studies of geometry, position and distribution of the salt layers, salt domes and/or salt walls are often hampered by their deep-seated position of a few kilometres in the upper crust. They were deposited tens of millions of years ago, often having had a long deformation history. In contrast, the salt structures in the Dead Sea Basin (DSB) provide a good opportunity to study the extension and the evolution of salt diapir within a relative simple and well-constrained tectonic deformation regime. The DSB is divided into two subbasins, which are separated by the Lisan Peninsula, a large buried salt diapir with an average thickness of about 8.0 km (Al-Zoubi & ten Brink (2001); Al-Zoubi & Ben-Avraham (2002)). Because the northern subbasin is occupied by the saline Dead Sea with a bathymetry of about 300 m deep (Hall 1996), the northern basin is less investigated, while the southern subbasin has been explored and investigated intensively over the last two decades (Ten Brink *et al.* 1993; Ginzburg & Ben-Avraham 1997; Al-Zoubi & Ben-Avraham 2002; Ben-Avraham & Schubert 2006; Weber & DESERT group 2009). The results of these investigations have indicated that the southern subbasin is deep, with more than 10 km of sedimentary infill (Al-Zoubi & Ben-Avaraham 2002; Ben-Avraham & Schubert 2006). Two large salt diapirs have been detected within this subbasin: the Sedom Diapir (Mt. Sedom in Fig. 1), and the elongated Lisan Diapir which has dimensions of about 15 km by 10 km and lies between Boqeq (line Number 8 in Fig. 1) and the En Gedi Fault (line Number 9 in Fig. 1, Al-Zoubi & Ben-Avraham 2002; Ben-Avraham & Schubert 2006).

The DSB is also the largest basin (Garfunkel 1981) within the Dead Sea Transform system (DST), which forms an intercontinental boundary between the Arabian and the African Plate (Fig. 1). It is defined as a left lateral strike-slip fault system with a length of around 1000 km, extending from the Red Sea in the south to the Taurus Mountains in Turkey (Garfunkel 1981; Reilinger *et al.* 2006; Weber & DESERT group 2009). Although the tectonic history and strike-slip movement of the DST fault have been well documented (e.g. Garfunkel 1981; Weber & DESERT group 2009), debate has continued over the past two decades concerning details of the tectonic system in place along the DST fault system, in particular with

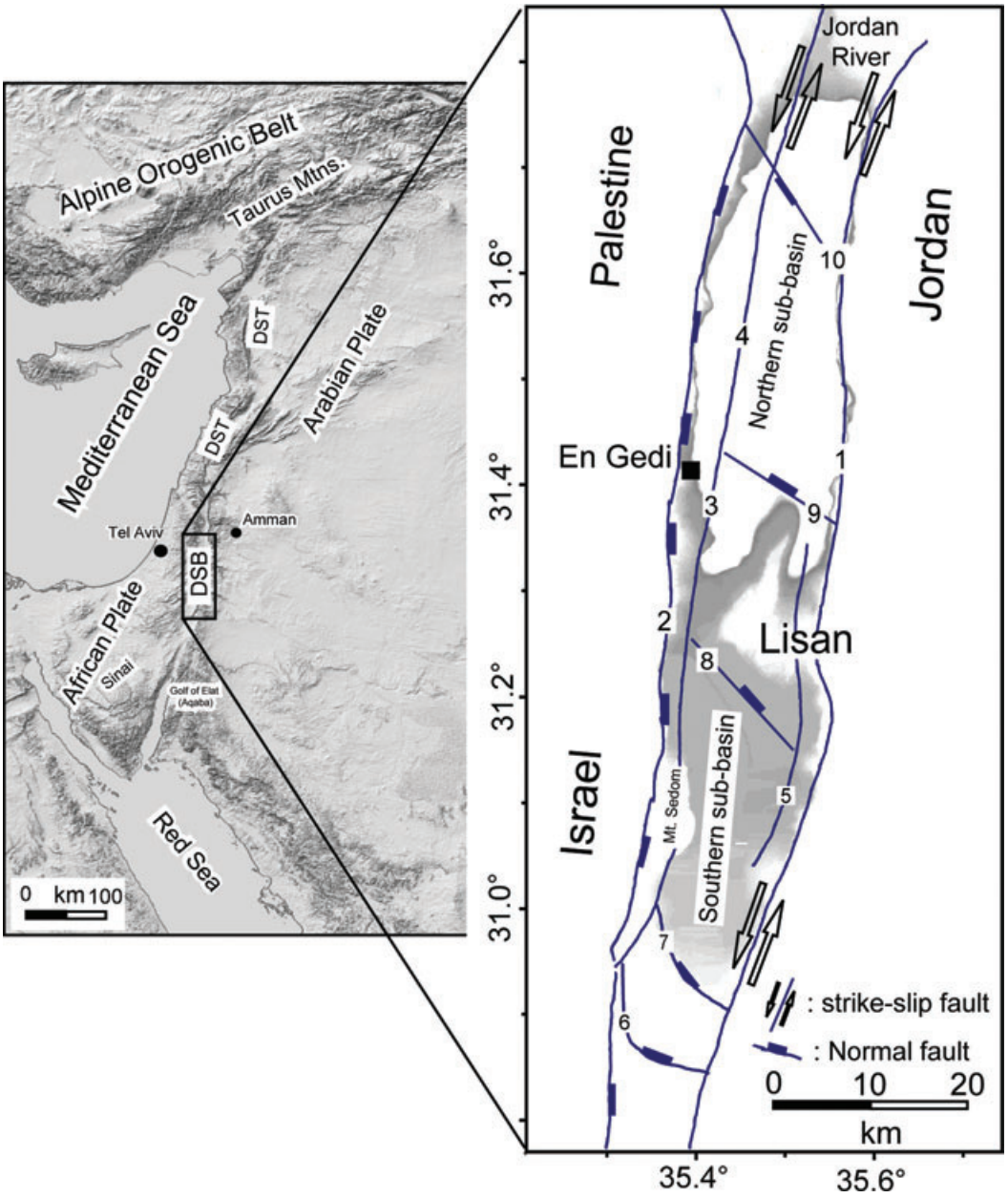

Figure 1. Digital Terrain Model of the Dead Sea Transform (DST) fault system: The DST fault system spans around 1000 km from the Red Sea in the South to the Taurus Mountains in Turkey. The Dead Sea Basin (DSB) is located in the inset, within the DST fault system. The main faults of the DSB are taken from different sources, redrawn after Gardosh *et al.* (1997) and Garfunkel & Ben-Avraham (1996). Fault lines are numbered as follows: Araba (Arava) Fault or Eastern boundary Fault (1), Western boundary fault (2), Sedom Fault (3), Jericho Fault (4), Ghor-Safi Fault (5), Iddan Fault (6), Khunaizira (Amazyahu) Fault (7), Boqeq Fault (8), En Gedi Fault (9) and Kalia Fault (10).

respect to (1) how large-scale transform fault systems are initiated, and (2) how such structures are typically expressed? The geoscientific DESIRE project (Dead Sea Integrated Research), comprised of partners from Germany, Israel, Palestine and Jordan, set out to tackle these questions (Petrunin & Sobolev 2008; Mechie *et al.* 2009; Götze *et al.* 2007, 2010).

One of the DESIRE project components was the aero gravity survey (Götze *et al.* 2010), which covered the central part of the DSB from the Red Sea to the northern margin of the Dead Sea. The main advantage of helicopter-borne gravimetry is the highly flexible survey flight planning and optimization. The survey altitude was as low as safely possible (approximately 200 m above the ground) to obtain the highest possible resolution, bearing in mind the extreme variations in elevation associated with the topography of the DSB (the Dead Sea lies more than 400 m below sea level, while the shoulders of the DSB are more than 1500 m high). Because the flight lines are covering the entire DSB independent on political boundaries (e.g. the boundary between Israel, Palestine and Jordan in our study area), the survey allows us an opportunity to get a homogenized gravity data set for the entire DSB.

The interpretation of the helicopter campaign results will focus on the following items. (1) modelling of near-surface structures in the northern subbasin, beneath the Dead Sea, (2) extension of salt diapirism in the northern subbasin and (3) hypothetical relationship between the spatial distribution of salt diapirism and earthquakes in the DSB.

The gravity research will contribute to a clarification of the mentioned points by 3-D constrained gravity modelling and combined interpretation.

2 TECTONIC AND GEOPHYSICAL FINDINGS AS CONSTRAINTS FOR THE MODELLING

To obtain direct evidence on the thickness and structure of the sedimentary section within the DSB, seismic wide angle reflection/refraction profiling has been conducted along the southern subbasin (Al-Zoubi & Ben-Avraham 2002) and across the Lisan peninsula (Mechie *et al.* 2009). The results indicate that the Cambrian crystalline basement lies at a relatively shallow depth (6–8 km) under the subbasin (Al-Zoubi & Ben-Avraham 2002). The En Gedi Fault (line Number 9 in Fig. 1) was detected in the south of the northern subbasin, which downthrows the basement and the overlying Cretaceous and pre-Cretaceous sediments to the south by about 4–5 km and forms the northern boundary of the southern subbasin (Al-Zoubi & Ben-Avraham 2002). This faulting was followed by the deposition of over 8 km of Pliocene to recent sediments, resulting in a 14 km thick sequence in the Lisan Peninsula area. Due to the exceptionally deepness of the sedimentary basin in this area with a couple of well defined boundary faults, it has been suggested that the southern subbasin is a drop-down basin (Ben-Avraham & Schubert 2006; Ben-Avraham *et al.* 2010). The Khunaizira (Amazyahu) Fault (line Number 7 in Fig. 1) is interpreted as a NW–SE trending normal fault, forming the southern margin of the southern subbasin. The Boqeq Fault (line Number 8 in Fig. 1) is also a NW–SE trending normal fault similar to the Khunaizira (Amazyahu) Fault, both of which cut through the deeper part of the sedimentary infill and into the basement (Ben-Avraham & Schubert 2006). In contrast, interfaces in the lower crust below about 20 km depth have been estimated by the DESIRE wide angle seismic interpretation (Mechie *et al.* 2009) to indicate a throw of less than 3 km. Thus the DSB is suggested to be an upper crustal feature resulting from upper crustal extension associated with the left-lateral motion along the DST fault system (Mechie *et al.* 2009). The boundary between the upper and lower crust at about 20 km depth has acted as a decoupling zone. Below of it the two plates moved past each other and cause a shear motion (Mechie *et al.* 2009).

The interpretation of the local seismicity of the DSB (Aldersons *et al.* 2003) indicated that well-constrained earthquakes display continuous focal depth down to the Moho at depth of 32 km, which require a cold lower crust and are consistent with the measured heat flux in the DSB (Föster *et al.* 2007). Local earthquake occurrences at depths of around 20 km are concentrated in the central part of the DSB between the Lisan peninsula and the En Gedi Fault, and along the Kalia and Khunaizira (Amazyahu) transverse faults (red triangles in Fig. 2; Hofstetter *et al.* 2000; Aldersons *et al.* 2003). Because shallower earthquakes at depths less than 10 km (blue triangles between the En Gedi and Boqeq Fault, Fig. 2) follow the margin of the Lisan peninsula (orange line in Fig. 2) to some extend, Aldersons *et al.* (2003) and Hofstetter *et al.* (2000) inferred that these shallower earthquake occurrences can be associated with the uplift and displacement processes of salt diapir in the Lisan peninsula. The salt layers are characterized by higher seismic velocities and lower densities than the adjacent sedimentary infill, as shown in Table 1 (Al-Khalidi *et al.* 1997; Rybakov *et al.* 1999). The mentioned findings and observations will be used to constraint the 3-D density modelling.

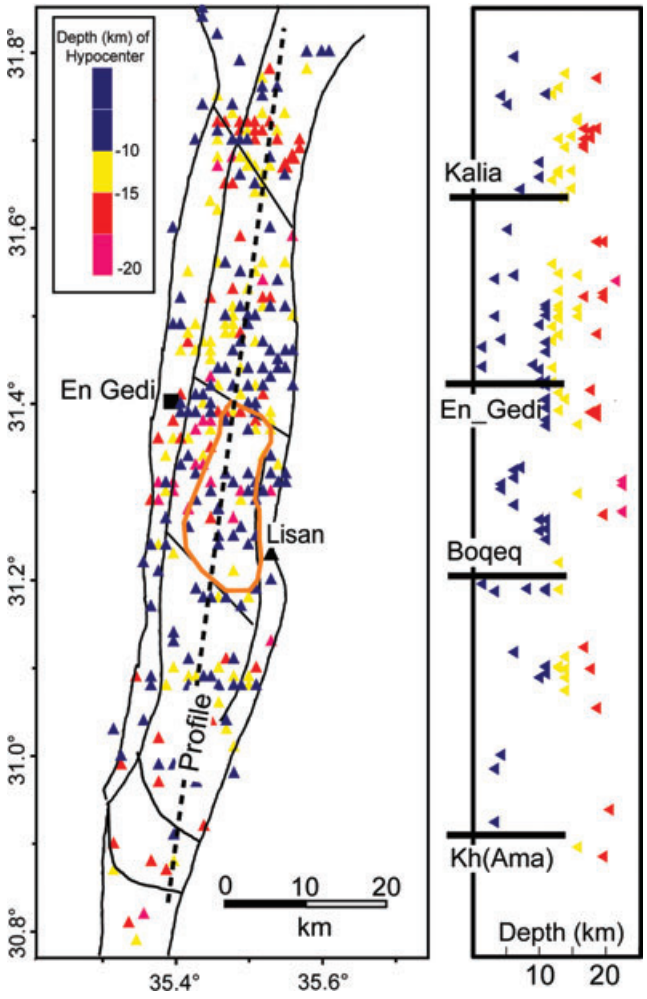

Figure 2. The depth distribution of earthquake hypocentres for the period 1981–2004 (Hofstetter *et al.* 2000, EMSC 2004) shows that the earthquake occurrences are concentrated in the central part of the DSB between the Lisan peninsula and the Dead Sea. Orange line indicates the Lisan salt diapir (Al-Zoubi & Ben-Avraham 2002).

Table 1. *P*-wave velocities and densities for the geological units, from seismic and borehole experiments (Al-Khalidi *et al.* 1997; Rybakov *et al.* 1999).

Stratigraphy	Seismic velocity (km s^{-1})	Density (kg m^{-3})
Pleistocene–Holocene sediment	< 4.0	2200–2300
Pliocene Salt diapir	4.4	2150
Miocene sediment	4.5	2300–2400
Mesozoic sediment	4.5–5.0	2400–2500
Paleozoic sediment	4.5–5.0	2600–2700
Cambrian basement	> 5.0	2700–2750

3 AVAILABLE GRAVITY DATA SETS AND DATA COMPILATION

3.1 Ship measurements in the Dead Sea

The terrestrial gravity stations shown in Fig. 3 resulted from the cooperative projects between Germany, Jordan and Israel. In 1988 October 300 km of marine gravity data were collected in the Dead Sea using the Lamont–Doherty Earth Observatory's BGM-3 marine gravimeter, which has a documented accuracy of better than

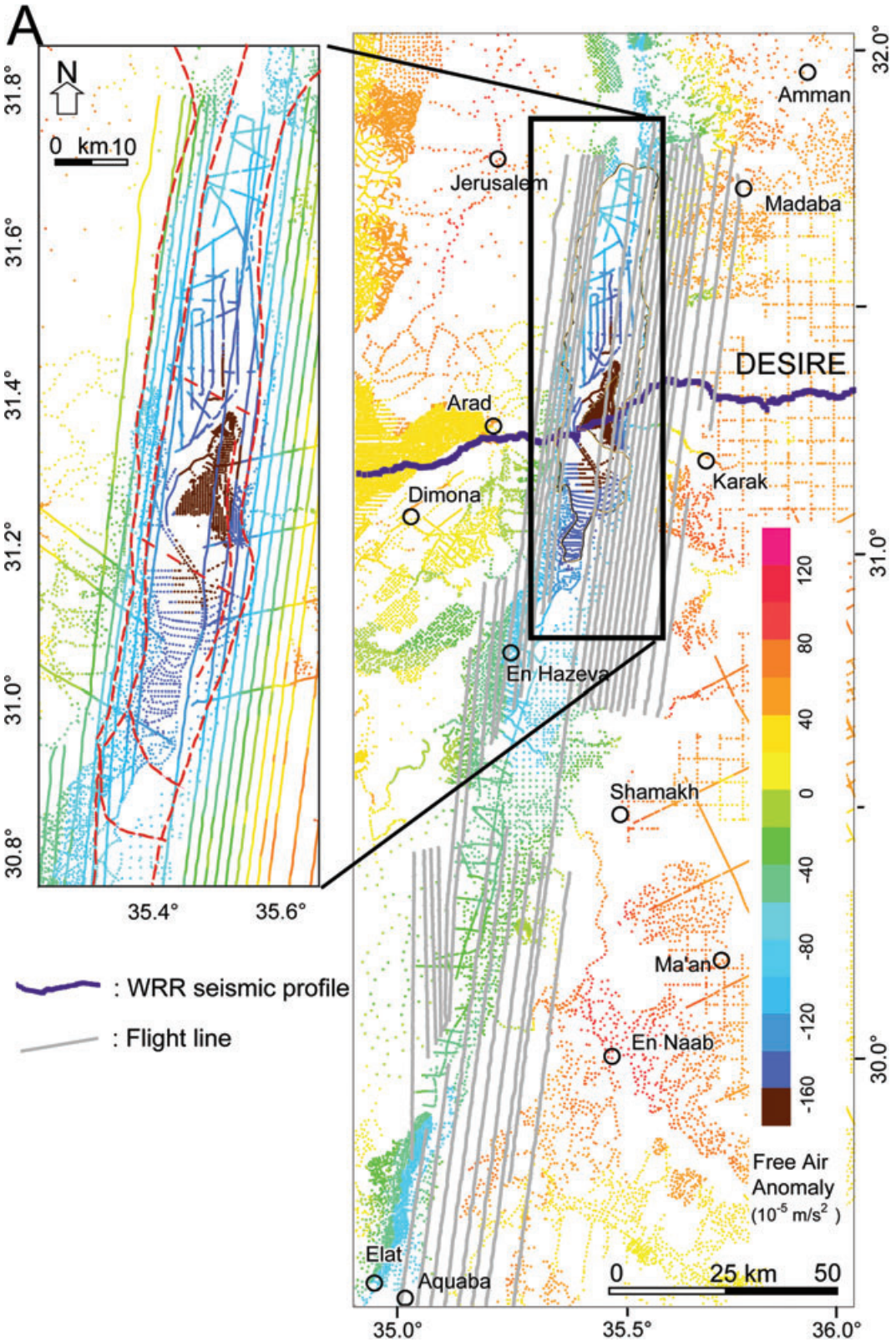

Figure 3. Flight lines (grey lines) and stations of the conventional gravity data (ten Brink *et al.* 1993; Hassouneh 2003; Götze *et al.* 2007, 2010). The DESIRE airborne survey covered the central part of the DSB, from Aquaba up to the northern part of the Dead Sea, as well as gaps in the terrestrial gravity data, mainly on the Jordanian side of the DSB. The DESIRE wide-angle refraction/reflection seismic profile (blue line) (Mechie *et al.* 2009) is also shown. The Dead Sea Basin study area is framed in a box (inset A). Red dotted lines in A indicate fault lines.

1.0×10^{-5} m s^{-2} (Ten Brink *et al.* 1993). Gravity observations were continuously done during three days and one night at an average speed of five knots recorded at 1 s intervals and monitored directly on the boat. A portable radar-ranging system of the Israel National Oceanographic and Limnological Institute supported the navigation every 1 s. Three base stations were located with distances of 10–15 km at the western shoreline of the Dead Sea. The positional accuracy of the system was 3 m. A moving average filter with a 200 s Gaussian window was applied to the marine gravity data to remove the boat accelerations. The data were manually edited to remove erroneous measurements and combined with the navigation (Ten Brink *et al.* 1993). The drift of the gravitymeter was negligible over the short period of the survey. Eötvös correction has been applied to compensate effects of the ship's movement. The accuracy of the shipborne measurements, after adjusting for internal consistency between crossing line, was 1.5×10^{-5} m s^{-2}. The sea level during data acquisition (1998 October 10–13) was 408.13 m below the sea level of the Mediterranean (Ten Brink *et al.* 1993).

3.2 Ground measurements at the Lisan peninsula

To get more information on surface deformations, which result occasionally in the generation of sink holes and subsidence in and adjacent to the Lisan peninsula, land gravity surveys were completed between the years 1989 and 1993 (Hassouneh 2003; Closson & Abou Karaki 2010). During these surveys gravity readings were recorded at more than 835 stations with a spacing of 20–250 m and an accuracy of approximately 0.01×10^{-5} m s^{-2}. The survey was carried out by a Scintrex Automated gravitymeter (CG3). The sea and land gravity data sets—prior to the airborne gravity survey—were reprocessed and homogenized using the 1967 Geodetic Reference system and the standard density of 2670 kg m^{-3} (Hassouneh 2003).

3.3 Helicopter-borne gravity survey

As already mentioned in the introduction the aero gravity survey covers areas, where terrestrial gravity data were not available (refer to Fig. 3 for flight lines). The helicopter which is owned by Federal Institute for Geosciences and Natural Resources (BGR, Hanover, Germany), was equipped with four geodetic GPS receivers, two inertial motion units and a laser scanner and a gravitymeter (GT-1A). For more details refer to Götze *et al.* (2010). Flights were performed in a height of approximately 200 m above ground to ensure the highest resolution, considering the extreme elevation differences associated with the topography of the DSB. For initial data processing a 100 s filter was used, resulting in a spatial resolution of approximately 1.6 km half-wavelength. In total, 2100 profile kilometre were flown during 18 flight hours in Israel and 4400 km during 21 h in Jordan. The data levelling (only zero- and first-order trend applied) minimized intersections error to 2.0×10^{-5} m s^{-2}, and the difference between the airborne and the terrestrial data to $3.5 \pm 4.0 \times 10^{-5}$ m s^{-2}. For the compilation of boat, terrestrial and airborne gravity data, we downwarded the airborne gravity data from the approximately 200 m flight level to the current topography which is represented by a 25 m grid (Rybakov, private communication, 2009) in the area of the DSB.

3.4 Topography and gravity variations in the DSB

The water level in the Dead Sea decreased approximately 80 cm yr^{-1} between the years 1988 and 1999, and about 100 cm yr^{-1} since 1999 (Yechieli *et al.* 2006). The sea water level in 2007 was at about 421 m below sea level (http:israмar.ocean.org.il). This recession of the water level is not only the result of natural factors (e.g. decreasing inflows from the Jordan River and increasing evaporation due to global warming) but is also a result of human factors such as the growing population along the Dead Sea coast and increased industrial activities (Yechieli *et al.* 2006). On the other hand, the ground level of the Lisan Peninsula is rising, which is caused by uplifting of the salt diaper there (Shimoni *et al.* 2002; Yechieli *et al.* 2006). Analysing InSAR interferometry data (ERS1/2) from 1997 July to 1999 March, Shinomi *et al.* (2002) and Baer *et al.* (2002) calculated uplift and subsidence rates of the Lisan peninsula. These authors noted that the shore subsidence appeared along the northern peninsula margins with a rate of 4.4 cm yr^{-1} and the uplifting rate was about 1.7 cm yr^{-1} in the time period between 1997 and 1999.

In comparison of our airborne and the terrestrial free air anomaly (Hassouneh 2003), we found significant anomaly differences of some -8.0×10^{-5} m s^{-2} in the Dead Sea area (Fig. 4). The differences are mainly due to the decrease of sea level of about 15 m in the time between 1988 and 2007. The sea surface lowering of 15 m is equivalent to a change of approximately 5.0×10^{-5} m s^{-2} of free air correction (0.3086×10^{-5} m s^{-2} $\times$ 15 m) between 1988 and 2007. This is the time period between the shipborne measurements (Ten Brink *et al.* 1993) and the airborne survey (Götze *et al.* 2010).

3.5 Data compilation

The compilation of Bouguer anomalies consists of the described data sets: (1) local ship measured gravity data (Ten Brink *et al.* 1993), (2) terrestrial gravity data by the Natural Resources Authority of Jordan (Hassouneh 2003), (3) ground measured gravity data by the Geophysical Institute of Israel (Rybakov, private communication) and (4) the DESIRE airborne gravity data as described above. In total, we combined approximately 20 000 shipborne, ground and airborne measurement stations, covering the DSB and adjacent areas. All stations are reprocessed by using the 1967 Geodetic Reference system and the standard density of 2670 kg m^{-3} for all continental masses and 1280 kg m^{-3} for the Dead Sea water, which was calculated from its salinity and temperature (Fonofoff & Millard 1983). The homogenized gravity field is linked to the IGSN71 gravity datum. Terrain corrections were calculated up to Hayford zone O_2 (167 km), using the digital elevation model with a 25 m grid (Geological Survey of Israel, Rybakov, private communication). The average accuracy of the Bouguer anomaly values is estimated to be 2.3×10^{-5} m s^{-2}. Fig. 5 shows the combined Bouguer anomaly map for the DSB with contour intervals of 10×10^{-5} m s^{-2}, based on a 1 km $\times$ 1 km grid. All anomalies range from almost zero, such as on the northwestern margin of the DSB, to -140×10^{-5} m s^{-2} (the most negative anomaly in the Middle East) in the centre of the Lisan Peninsula. This minimum extends northwards into the centre of the Dead Sea and southwards into the southern subbasin.

4 INTERPRETATION AND ANALYSIS OF THE GRAVITY FIELD

4.1 Wavelength filtering

To analyse the Bouguer anomaly a wavelength filtering has applied for gravity field separation. The influence of deep-seated bodies on gravity causes regional (long wavelength) variations in the gravity

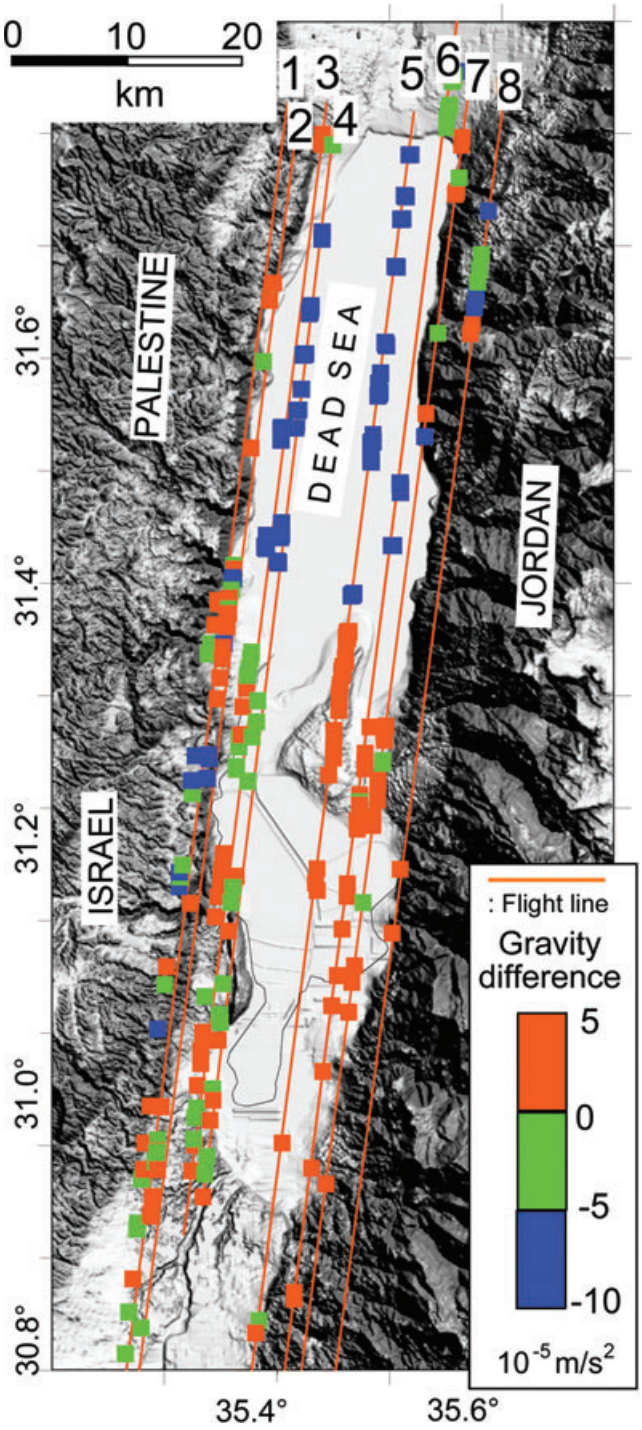

Figure 4. Gravity difference between the airborne and the conventional gravity data sets. Comparing the airborne to the conventional free air anomaly data set, we found significant anomaly difference (airborne–conventional free air anomaly) of about -8.0×10^{-5} m s^{-2} over the Dead Sea area, which is mainly due to the sea level having lowered by about 15 m in the duration between 1988 and 2007. Flight lines are numbered as follows: IS09N-2 (1), IS07N-2 (2), IS08N-1 (3), IS08N-2 (4), JO09N-2 (5), JO15N-4 (6), JO10N-1 (7) and JO11N-1 (8).

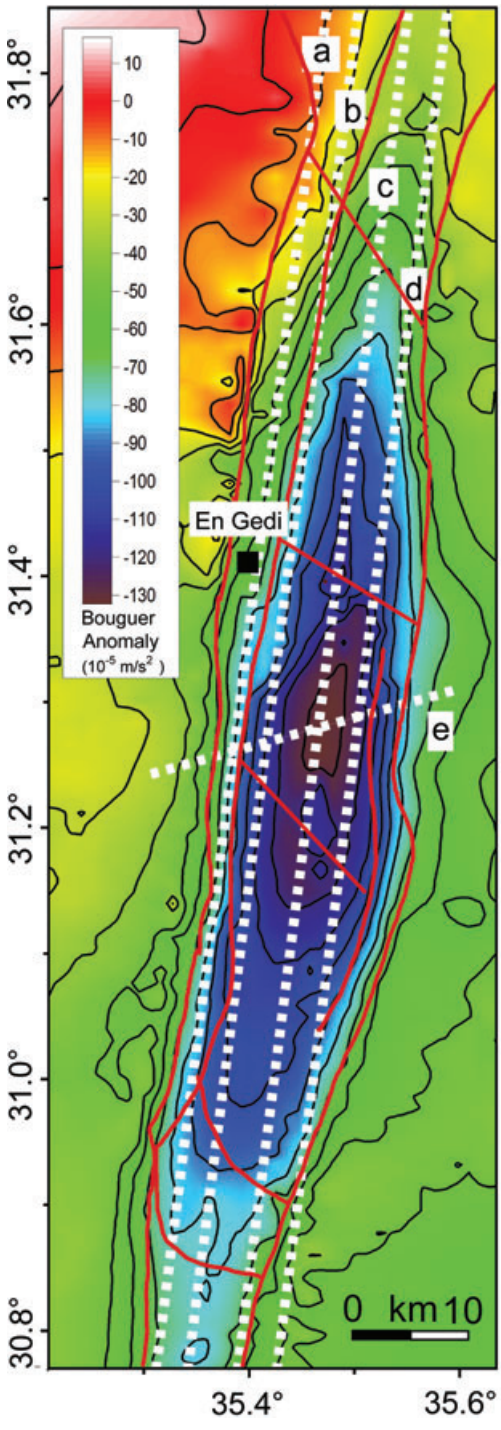

Figure 5. Bouguer anomaly map over the DSB, with a constant grid size of 1 km, interpolated from the compiled gravity data set (Fig. 3). Red lines are the fault lines. The white dotted lines (a, b, c and d) indicate positions of the N–S model profiles (see Fig. 12) along the flight lines (IS07N-2, IS08N-2, JO09N-2 and JO10N-1, see also Fig. 4) and E–W cross-section (see Fig. 11) along the DESIRE seismic profile (Mechie *et al.* 2009).

field. They are often removed to highlight residual (short wavelength) anomalies, which are caused by shallow bodies (e.g. salt diapir in the DSB in our research). The relation between an effective wavelength (L_{ef}) and a maximum source depth (T_{max}) is defined by the equation ($L_{ef} \approx 3 \times T_{max}$, Degro 1986). Because we are interested on the gravity effect of the contrasting sediment infill (thickness: 12 km, density: 2400 kg m^{-3}) and the basement (thickness: 10 km, density: 2700 kg m^{-3}), we calculated a regional field using with an effective wavelength (L_c) of 35 km, which is corresponds approximately of three times of the sediment thickness.

After subtracting this regional field from the Bouguer gravity field, the residual field is mainly caused by density inhomogeneities of the sediment infill down to a depth of 12 km.

Fig. 6A shows that the regional field along the longitudinal axis of the basin decreases from both the northern and southern rims towards the centre (see also the red profile line in Fig. 6C which portrays the regional trend along the profile A). This has led to the assumption that the basin gradually sags towards the centre and that the deepest area in the DSB is located beneath the Lisan Peninsula. This was also observed in previous gravity and seismic interpretations (Ten Brink *et al.* 1993; Al-Zoubi & ten Brink 2001; Mechie *et al.* 2009). The positive values of the residual field (Fig. 6B) are located along the western and eastern boundary fault lines (follow the blue line in Fig. 6D). They indicate significantly density contrasts between the sedimentary infill in the DSB and the rocks of the adjacent areas. In addition, small positive residual anomalies are consistent with the locations of transversal fault lines (e.g. En Gedi in Fig. 6C), which means that the density contrasts are mainly caused by a tectonic faulting process. The negative residual field in the Lisan peninsula area should be caused by lower density material than the sediment infill (2400 kg m^{-3}). They correlate with the distribution of a salt diapir with an average density of 2150 kg m^{-3} (Table 1) as shown in Fig. 6C. The low residual anomalies in the Dead Sea can be explained by the Dead Sea water column, which has a density of 1280 kg m^{-3} (Fonofoff & Millard 1983) and an average thickness of 300 m (Hall 1996).

4.2 Curvature analysis

To enhance imaging of the gravity field caused by prominent subsurface density discontinuities (e.g. tectonic boundaries and the rim of salt diapir in the DSB), we applied 'dip curvature' analysis. Curvature analysis was applied for the interpretation of 3-D seismic arrays (Roberts 2001) and has been already tested to gravity data (e.g. Schmidt & Götze 2003). Curvature analysis is particularly useful for enhancement of linear elements, (e.g. gravity lineaments of the residual field) and it helps to identify orientations of such elements. The power of curvature analysis lies in the fact that it is a surface-dependant attribute and, thus, provides insight into surface properties that are intrinsic to that surface and difficult to express otherwise.

To get a better understanding curvature calculation of gravity field, a basic concept is given in Fig. 7. A gravity curve in the plane (Fig. 7A), which is caused by the density contrast in the crust (e.g. density difference between RHO1 = RHO3 > RHO2, Fig. 7B) can be thought of as a consecutive string of arcs of a circle characterized by variable centres and radii. Therefore, the curvature (k) at any given point on this curve can be defined as the reciprocal of the radius (R in Fig. 7A) of a particular arc segment at that point. It can also be defined as the derivative of the curve's tangent (T in Fig. 7A) with respect to its position on the curve at that point. In other words, if $\omega(s)$ is the angle of the curve with respect to a reference axis as a function of the path length (s) of a specified curve segment, then $k = d\omega/ds$ (Fig. 7A). Curvature k can be determined directly by evaluating the derivative $d\omega/ds$ as follows: $k = [\frac{dY^2}{dX^2}]/\mathrm{SQRT}[1 + (\frac{dY}{dX})^2]^3$(Roberts 2001). From the equation above, the curvature can be simply defined as the second derivative, $k = d^2Y/dX^2$ (e.g. Fig. 7D). A sense for both the sign and magnitude of curvature of any curve can be obtained by replacing the radii by vectors normal to the curve. Following the convention proposed by Roberts (2001), normal vectors illustrate the curvature. It follows that planar surfaces have zero curvatures (e.g. yellow or green colours in Fig. 7D), antiformal curves have positive curvatures (red lines in Fig. 7D) and *syn*-formal curves display negative curvatures (blue line in Fig. 7D), which both can be caused by distinct structural dislocations and density contrasts. Consequently, the calculation of curvature can be expected to furnish information on crustal density structures, which cause gravity anomalies.

The 'dip curvature' of the Bouguer anomaly in the DSB was calculated using an in-house JAVA program based on algorithms published by Roberts (2001). Fig. 8A shows the mapped 'dip curvature', which is calculated in the direction of the largest dip of the combined gravity surface (Roberts 2001). As mentioned above, the pronounced pairs of positive- (red colours in the Figs 8A, B and C) and negative values (blue colours in the Figs 8A, B and C) of the dip curvature indicate areas, where are characterized by strong density contrasts in the crust. (1) the pair of values numbered with 1 and 2 as well as the pair with 3 and 4 (Figs 8A and B) are correlated with locations of the western and eastern boundary fault lines (EBF and WBF in Figs 8A and B), respectively. We interpreted that they are caused by prominent density contrasts between the sedimentary infill in the DSB and the rocks of the adjacent areas. (2) The pairs of negative and positive dip curvature values revealed along the longitudinal profile line (Fig. 8C) are consistent with the locations of transversal fault lines, which mean that tectonic faulting processing cause density contrasts of subsurface crustal structures. (3) Along the western rim of the Lisan Peninsula, strong dip curvature values form a lineament (line number 6 in Fig. 8A) running from Sedom area to the northeastern edge of the Lisan peninsula, which should be caused by the density contrast between the salt diapir (2150 kg m^{-3}) and the sediment infill (2400 kg m^{-3} in Tables 1 and 2). (4) Another strong curvature lineament is observed in the central part of the Dead Sea (line number 7 in Fig. 8A). We interpreted this lineament as reflecting gravity anomalies caused by shallow seated density inhomogeneities of unknown origin beneath the Dead Sea. In addition, we suggested that strong curvature lineaments revealed outside of DSB (e.g. lineaments numbered with 8 and 9 in Fig. 8A) are due to density inhomogeneities in sediment infill (e.g. density contrast between Miocene- (2350 kg m^{-3}) and Paleozoic sediment (2650 kg m^{-3} in Table 1).

4.3 Euler deconvolution

To get preliminary information on the distribution of 3-D source-locations in the DSB prior to 3-D forward modelling, the well-known Euler deconvolution (Thomson 1982; Reid *et al.* 1990; Pašteka *et al.* 2009) has been applied to Bouguer anomalies. Euler deconvolution technique has been applied to potential field data for more than 20 yr (Thomson 1982; Reid *et al.* 1990; Pašteka *et al.* 2009), and help to speed up interpretations of potential fields in areas of simple density distributions (e.g. dyke like or other isolated structures). The degree of homogeneity N in the Euler equation can be interpreted as a structural index (SI), which is a measure of the rate of change with distance of a field (Pašteka *et al.* 2009)

(1) Centre of mass point (SI = 2),
(2) Centres of dyke-like features (SI = 1) and
(3) Position for the top of dyke-like feature (SI = 0, e.g. tectonic boundary).

Pašteka *et al.* (2009) introduced regularized derivatives for the 3-D Euler equation which based on the Tikhonov approach. The

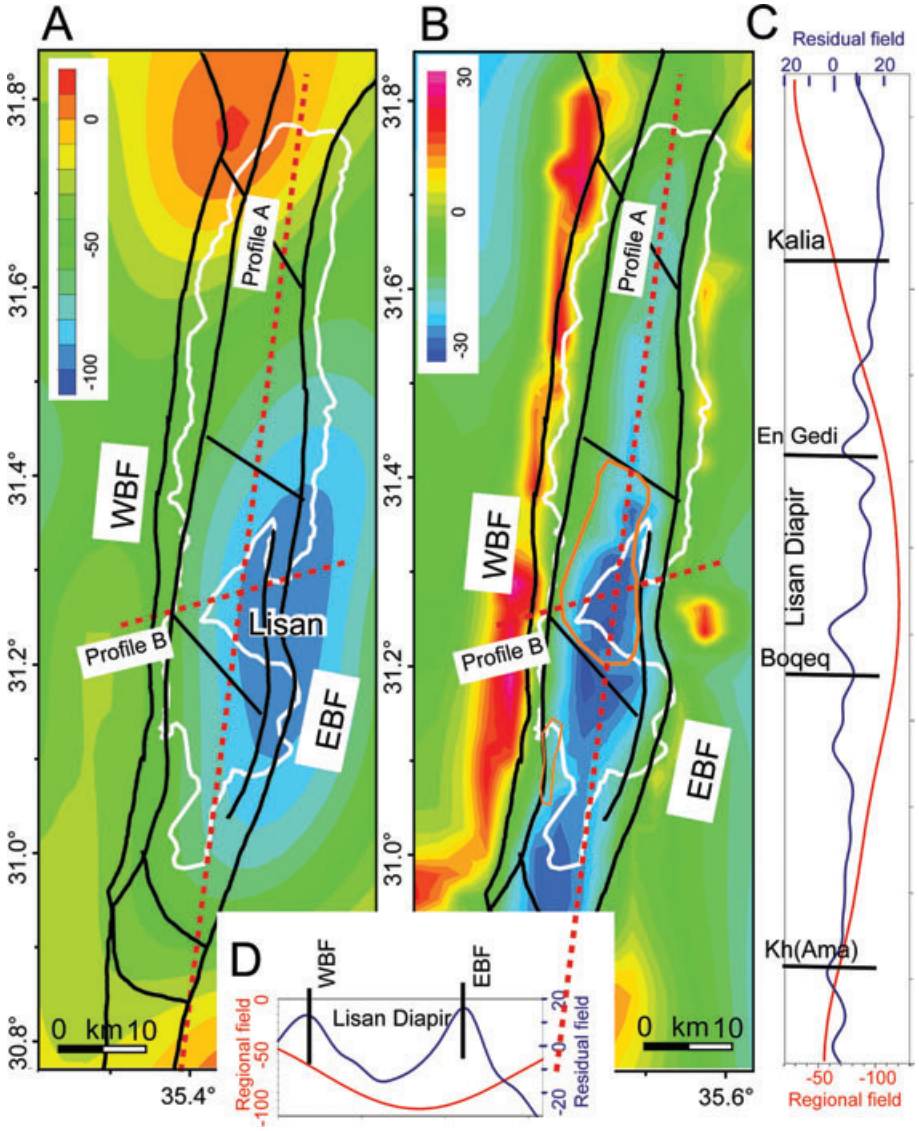

Figure 6. Regional (A) and residual (B) gravity field maps calculated using an effective wavelength of 35 km for the gravity field. 'A' shows that the regional field along the longitudinal axis of the basin decreases from both the northern and southern ends towards the centre (see also red line in C). The negative residual anomalies of about -30×10^{-5} m s^{-2} within the DSB as shown in B correspond to the distribution of salt diapir within the DSB. 'C' and 'D' show that the residual positive components correspond to the transversal and longitudinal faults. WBF, Western boundary Fault; EBF, Eastern boundary Fault. Orange lines are margins of salt diapirs, which are proposed by former geoscientific interpretation (e.g. Al-Zoubi & Ben-Avraham 2002).

calculation of derivatives is performed in the spectral domain by means of the Fast-Fourier-Transformation multiplied by the regularization filter for a selected (optimal) regularization parameter, which corresponds to a local minimum of the norm function. However, the norm function bases on real data, which usually leads to two or more local minima. In such case, the local minimum has to be selected by 'hand'. In many cases—such as ours—, this decision is a bit problematic. Two sets of solutions were obtained which were calculated with the in-house program REGDER which is described in greater detail by Pašteka *et al.* (2009). A set of solutions shallower source points at depths of 0.5–3 km (blue points, Figs 9A and B) and a set of deeper points at depths of 5–12 km (red points, Figs 9A and B). Pašteka *et al.* (2009) proposed to use SI = 2 for calculations of the density centres in the DSB, which are probably caused by the density difference between the upper crustal sediment infill (density of 2400 kg m^{-3}) and the Pre-Cambrian basement (density of 2700 kg m^{-3}). As shown in Fig. 9B, the depths of the centres (red points) vary from 8 km at the southern margin of the subbasin in the south to 12 km in the central part of the Lisan peninsula. In the Dead Sea area the depths of mass centres vary from 5 km near the northern rim of the Dead Sea to 8 km at the northern margin of the Lisan peninsula (Fig. 9B). This has led to the assumptions that the basin gradually sags towards the centre and the deepest area in the DSB is located beneath the Lisan Peninsula, as it was also obtained by the regional gravity filtering (Fig. 6A). The tops of density structures (blue dots in Figs 9A and B) were also calculated using SI = 0: results indicated that dyke-like density structures (caused by tectonic boundaries; Pašteka *et al.* 2009) are correlated with the location of longitudinal and transversal fault lines in the DSB as shown in Fig. 9B except the Boqeq Fault. This means that there is no prominent density contrast in the Boqeq Fault.

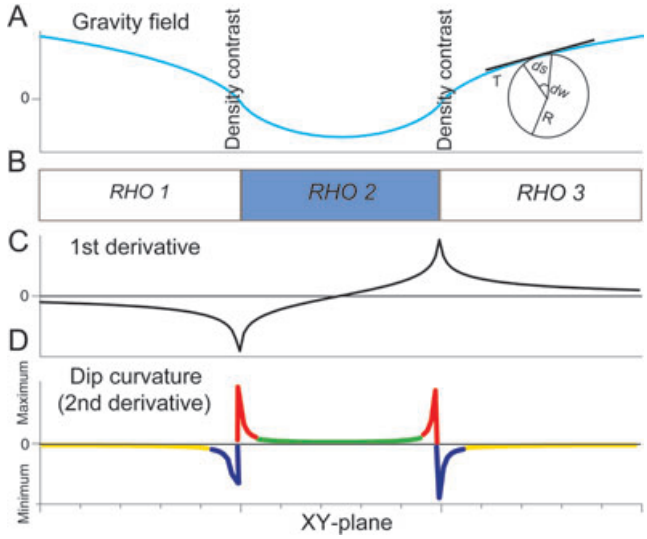

Figure 7. Conceptual illustration of the dip curvature analysis. A gravity curve in the plane (A), which is caused by the density contrast in the crust (e.g. RHO1 = RHO3 > RHO2, B) is thought of as a consecutive string of arcs of a circle characterized by variable centres and radii, *R*. It can also be defined as the derivative of the curve's tangent, *T* with respect to its position on the curve at that point (Roberts 2001). Curvature can be determined directly by evaluating the derivative $d\omega/ds$ (A) and defined as the second derivative (D). Planar surfaces have zero curvatures (yellow or green colours), antiformal curves have positive curvatures (red lines) and *syn*-formal curves display negative curvatures (blue line in D), which both can be caused by distinct structural dislocations and density contrasts.

5 3-D GRAVITY MODELLING

5.1 Methodology and constraining data

The software used for the gravity modelling was IGMAS 3-D modelling package developed by Götze (1984). IGMAS+ was later extended towards a modern interpretation system with GIS functionality today (Götze & Schmidt 2002; Schmidt *et al.* 2004, 2010). The kernel of the system uses polyhedrons with triangulated surfaces to approximate bodies of constant density and/or magnetic susceptibility within the earth's crust and mantle, the geometry of which is defined by a number of parallel vertical modelling sections (Götze & Lahmeyer 1988). The positions of the 37 vertical sections in the model used herein were chosen to be parallel to the flight lines, with south–north orientations (e.g. line marked by a, b, c and d in Fig. 5) running roughly along the DST fault system. The distances between adjacent vertical sections, varied between 200 and 2000 m depending on the underground complexity, were defined according to the modelling requirements for the combined Bouguer anomaly and topographic variation.

5.2 Constraints on geometry and densities

Interpretation of potential field data requires interdisciplinary knowledge and the integration of information from different types of independent data. IGMAS provides GIS functions to integrate other geophysical information from both geophysics and geology (Schmidt & Götze 1998; Götze & Schmidt 2002; Schmidt *et al.* 2004). Several independent constraints, obtained from geophysical, geological and tectonic interpretations, were taken into account.

(1) The positive residual gravity field shown in Fig. 6B and dip curvature calculations (Fig. 8) were used to estimate the density

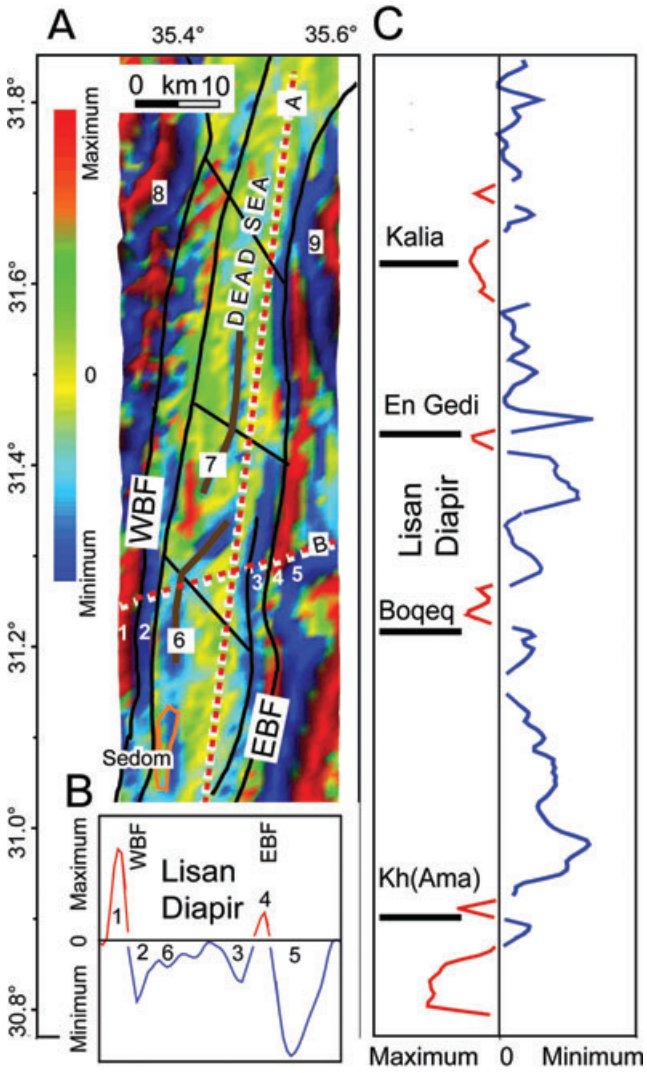

Figure 8. Dip curvature values (A) are calculated in the direction of the largest dip of the Bouguer anomalies in the DSB (Fig. 5). The pronounced pairs of positive (red colour) and negative values (blue colour) of the dip curvature are correlated with the location of the western (WBF) and eastern boundary fault lines (EBF, see also B). 'C' shows the strong correspondence between locations of transversal faults and the pairs of positive and negative values.

contrasts in the sediment infill, which are mainly associated with gradients to interpret the existing anomalies and sources for the observed gravity field within the sedimentary fill (Figs 10A and B).

(2) The set of Euler source points at depths of 0.5–3 km (blue points in Fig. 9 and Fig. 10C) was used to estimate the subsurface density structures in the upper crust. The set of deeper points at depths of 5–12 km (red points in Figs 9 and 10C) was used to estimate the depth to the contact between sedimentary fill and the basement in the upper crust, which is correlated with the velocity discontinuity from 6.0 to 6.4 km s^{-1}.

(3) To obtain direct evidence on thicknesses, structures and densities from the surface down to the Moho, the seismic wide angle refraction/reflection (WRR) profile obtained within the framework of the DESIRE project by Mechie *et al.* (2009, Fig. 10C) was used, together with density–velocity relationships from Sobolev & Babeyko (1994). The seismic profile shows velocity discontinuities under the Lisan Peninsula at depths of about 12 km (6.0–6.4 km s^{-1}), 20 km

Table 2. Model densities calculated from the DESIRE seismic velocity discontinuities (Mechie *et al.* 2009) using density–velocity relationships from Sobolev & Babeyko (1994).

Structure		Depth (km)	Velocity (km s^{-1})	Average density (kg m^{-3})
Upper crust	Sediment	Shallower than 12	Lower than 6.0	2400
	Basement	12–22	6.0–6.4	2700
Lower crust		22–32	6.7–7.2	2900
Mantle		Deeper than 32	Higher than 7.9	

(6.4–6.7 km s^{-1}) and 32 km (7.2–7.9 km s^{-1}). From these velocity discontinuities, we calculated the densities of modelled crustal structures shown in Table 2 (Fig. 10C).

(4) Depth distributions of earthquake hypocentres (Figs 2 and 10C, Hofstetter *et al.* 2000; Alderson *et al.* 2003; EMSC 2004) were used to detect fault lines and structural boundaries. The accuracy of the depth determination cannot exceed ±2 km (Alderson *et al.* 2003).

(5) The modelled structures in the upper crust were defined on the basis of previous geologic and gravity interpretations (e.g. Ben-Avraham *et al.* 2006, Fig. 10D).

(6) Density determinations obtained from boreholes and petrophysical research, were used to estimate subsurface model densities (e.g. Tables 1 and 2).

(7) Digital-Elevation-Model with a 25-m grid (Geological Survey of Israel, Rybakov, private communication) was used to define most superficial geometries.

5.3 Interpretation and results

Fig. 10F presents the final 3-D gravity model along a longitudinal flight line JO09N-2 (for the location, see profile c in Fig. 5), which has been modified using all available additional information such as the residual gravity field (Fig. 10A), curvature analysis (Fig. 10B), Euler deconvolution source points, distributions of seismic velocities, earthquake events (Fig. 10C) and former geophysical interpretations (e.g. Ben-Avraham & Schubert 2006, Fig. 10D). Positive components of the residual field and the dip curvature analysis are consistent with the location of transversal fault lines (e.g. the Khunaizira (Amazyahu)-, Boqeq-, En Gedi- and Kalia Fault). The negative residual anomalies, which are mainly revealed in the Lisan peninsula and the northern basin below the Dead Sea, correlate with the distribution of salt diapirism in the sediments. Comparing the local minimum curvature value in the southern margin of the southern basin (grey line 'a' in Fig. 10A, B and F) to the set of deeper points calculated by the Euler deconvolution (red points Fig. 10C), we interpreted this line as a fault line below the sediment, which is located in a depth of 7 km. The grey lines 'b' and 'c' (Fig. 10A, B and F) indicate probably density contrasts in the salt diapir in the Lisan peninsula. The distribution of deeper Euler source points leads us to estimate a crustal density contrast between the subsurface sedimentary infill and the Pre-Cambrian basement as proposed with black dotted line in Figs 10C and F. The upper crust in the DSB is composed of sediment and salt diapirism of Palaeozoic to recent age (Ben-Avrahan & Schubert 2006), overlying a crystalline basement that is reached at a depth of about 14 km in the Lisan Peninsula and about 10 km in the northern subbasin, which is deeper that the depth previously interpreted from seismic data (Al-Zoubi & Ben-Avraham 2002). The modelled densities were 2700 kg m^{-3} for the crystalline basement, 2620 kg m^{-3} for the Palaeozoic, 2470 kg m^{-3} for the Mesozoic, 2390 kg m^{-3} for the Miocene and 2250 kg m^{-3} for the recent sediments. The lowest gravity anomaly of approximately -140×10^{-5} m s^{-2}, observed in the area of the Lisan Peninsula (Fig. 10E), is well explained by the salt diapir which has a thickness of about 8 km, as indicated by seismic interpretation (Al-Zoubi & Ben-Avraham 2002, Mechie *et al.* 2009) and a density of 2080 kg m^{-3}. Since this density is lower than the density measurement from several boreholes (2150 kg m^{-3}, see Table 1), we infer that the salt diapir in the Lisan Peninsula includes a fluid component, such as salt water. The negative anomalies lower than -100×10^{-5} m s^{-2} observed over the Dead Sea locating between 80 and 110 profile-kilometre along the profile can be explained by the modelled body alone (labelled '1' in Fig. 10F), which is characterized by a density of 2080 kg m^{-3} and a thickness of about 4 km. The density of the modelled body refers to a salt diapir, which has not

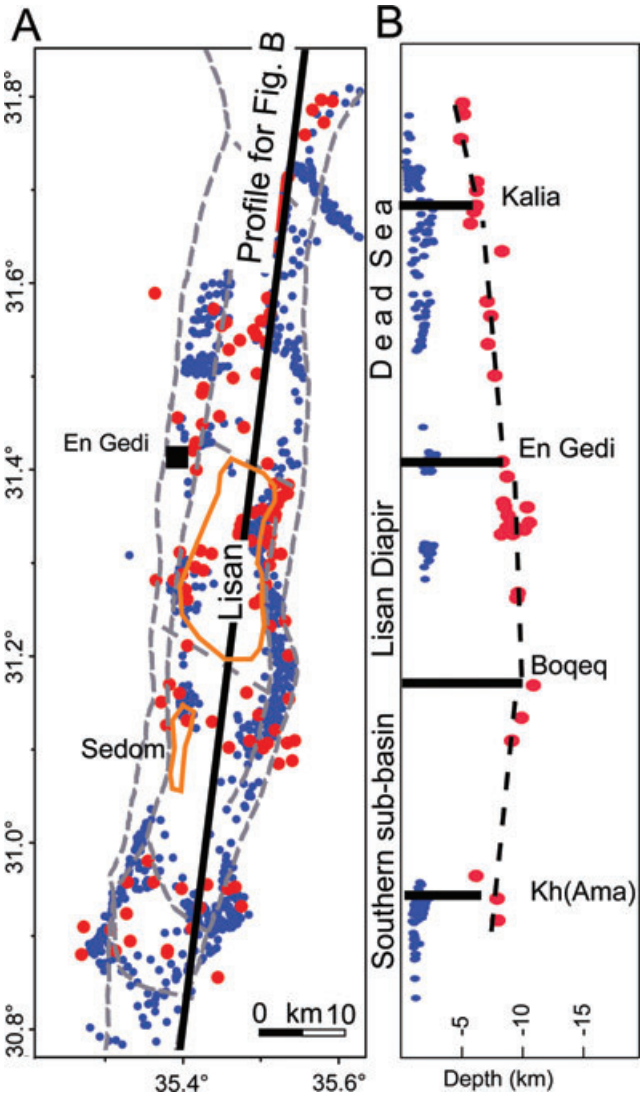

Figure 9. A set of solutions shallower source points at depths of 0.5–3 km (blue points) and a set of deeper points at depths of 5–12 km (red points). The shallower source points calculated using SI = 0 indicate that dyke-like density structures are correlated with the location of longitudinal and transversal faults in the DSB as shown in B except the Boqeq Fault. Orange lines indicate salt diapirs (Al-Zoubi & Ben-Avraham 2002)

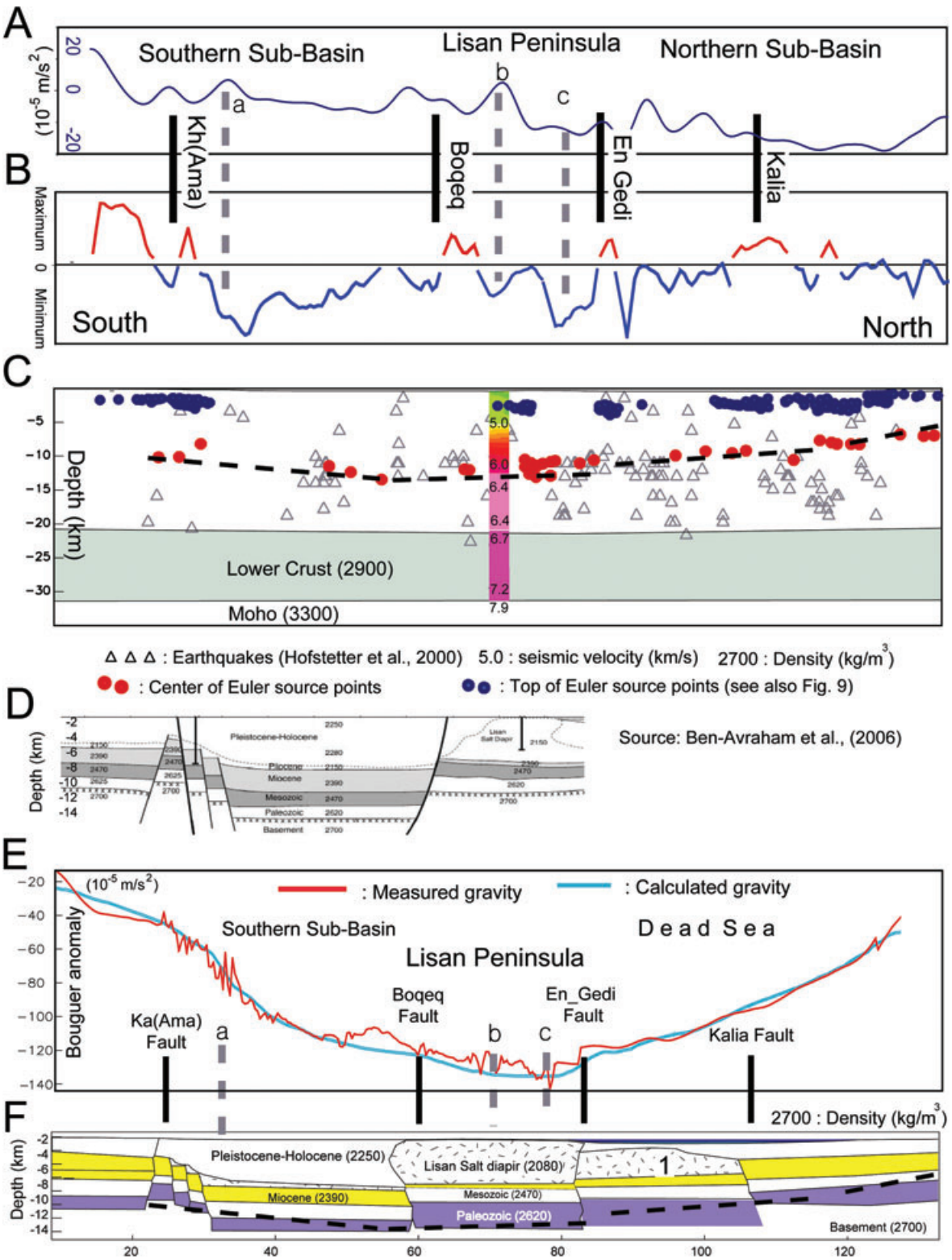

Figure 10. Constraints on geometry and densities along the model section c in Fig. 5, which are obtained from gravity interpretation by gravity residual field (A), curvature analysis (B), Euler deconvolution (blue and red circles in C), seismic velocity distributions (Mechie *et al.* 2009, coloured bar in C), earthquake distribution (Hofstetter *et al.* 2000; EMSC 2004, black open triangles in C) and previous gravity models (Ben-Avraham & Schubert 2006 in D). The grey lines 'a', 'b' and 'c' in A, B and F indicate locations of density contrasts in the sediment infill and salt diapir independent on fault lines. The lowest gravity anomaly of approximately -140×10^{-5} m s^{-2}, observed over the Lisan Peninsula (E) is well explained by the salt diapir, which is characterized by a thickness of about 8 km and an average density of 2080 kg m^{-3}, as modified in our final model (F). The negative anomalies lower than -100×10^{-5} m s^{-2} observed over the Dead Sea locating between 80 and 110 profile-kilometre can be explained by the modelled body alone (labelled '1'), which is characterized by a density of 2080 kg m^{-3} and a thickness of about 4 km.

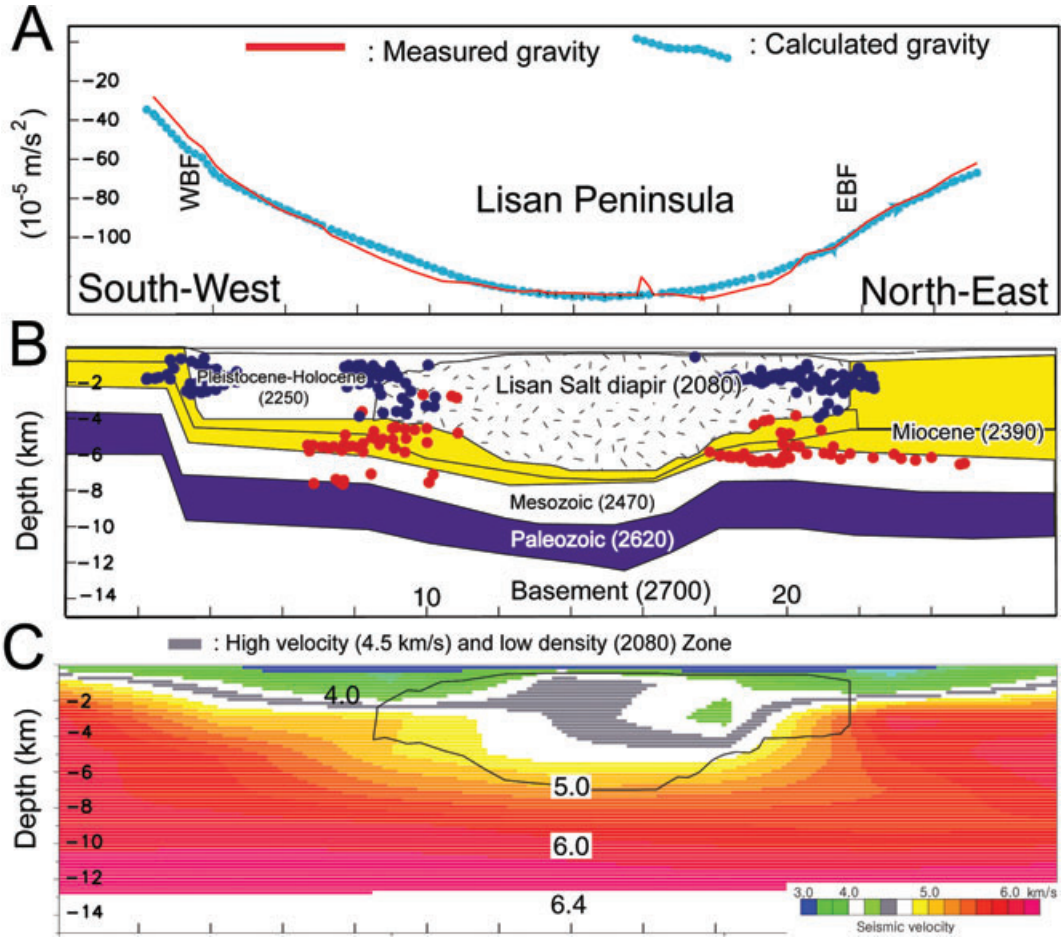

Figure 11. SW–NE vertical cross-section along the DESIRE seismic profile (see Fig. 5 line 'e' for location of the profile). The red and blue dots in 'B' are the source points for the Euler deconvolution of the gravity field (see also Fig. 9). The velocity distribution along the profile (Mechie *et al.* 2009; C) indicates that the large negative gravity anomaly over the Lisan Peninsula (A) is caused by the modelled Lisan salt diapir in B, which corresponds perfectly with the high velocity zone between 4.0 km s^{-1} and 5.0 km s^{-1} (white and grey area in C) within the sediment basin.

been recognized in any other geophysical interpretations. The top layer of the modelled salt diapir is about 2 km below the level of the Dead Sea, a depth which also is supported by Euler deconvolution (blue dots in Fig. 10C). The 2 km difference in depth between the top of the Lisan salt diapir and the top of the modelled salt diapir can be explained as being a result of normal faulting along the En Gedi Fault: the Lisan Peninsula, on the southwestern side of the En Gedi Fault has been uplifted, while the northeastern side of the fault has been down-thrown, forming the southern margin of the northern DSB.

In Fig. 11 we present a SW–NE section (for the location, see profile e in Fig. 5) along the line of the DESIRE seismic profile (Mechie *et al.* 2009), of which the gravity field is characterized by a low in the gravity anomaly of approximately -140×10^{-5} m s^{-2}, observed over the Lisan Peninsula (Fig. 11A). Euler source points calculated using SI = 0 to approximate the tops of the mass (blue dots in Fig. 11B) are concentrated along the faults and vicinities of the Lisan salt diapir. The Euler points calculated using SI = 2 (red dots in Fig. 11B) yielded mass centres at an approximate depth of 6 km. The deepest part of the basin along this profile is centred under the Lisan Peninsula, where the sedimentary basin has a thickness of about 14 km. The thickness of the salt diapir varies from about 8 km in the Lisan Peninsula to less than 4 km to the west and east. The modelled Lisan salt diapir corresponds well with the high velocity zone of about 4.4 km s^{-1} within the sedimentary basin (grey colours in Fig. 11C) that otherwise has an average velocity of 4.0 km s^{-1} (white colours in Fig. 11C).

In Fig. 12, four parallel sections are presented across typical parts of the final density model; their locations can be found in Fig. 5. The first section (Fig. 12a) along the flight line IS07N-2 shows the model for the western rifted margin of the DSB, the second section (Fig. 12b) follows the flight line (IS08N-2) 2 km to the east of the first section, the third section (Fig.12c) is along the flight line JO09n-2 (Fig. 12d, see also Fig. 10F) and the fourth section (Fig. 12d) is along another flight line (JO10N-1), which reveals the density structure on the eastern rifted margin of the DSB. The inferred salt diapir beneath the Dead Sea (labelled '1' in Fig. 12) extends only from the central part of the Dead Sea to the vicinity of its western bank, with a thickness that decreases from 4 km in the centre (Fig. 12c) to less than 1 km in the west (Fig. 12b). The thickness of the Lisan salt diapir (labelled '2' in Fig. 12) varies from about 8 km in its centre to about 3 km on its western and eastern edges. The salt diapir labelled '3' in Fig. 12b may extend from the southwestern part of the southern Dead Sea subbasin into the southeastern part, with a thickness decreasing from about 6 km to less than 1 km.

The model gravity that matches the Bouguer field in the DSB is given in Fig. 13A, and a comparison with the observed field

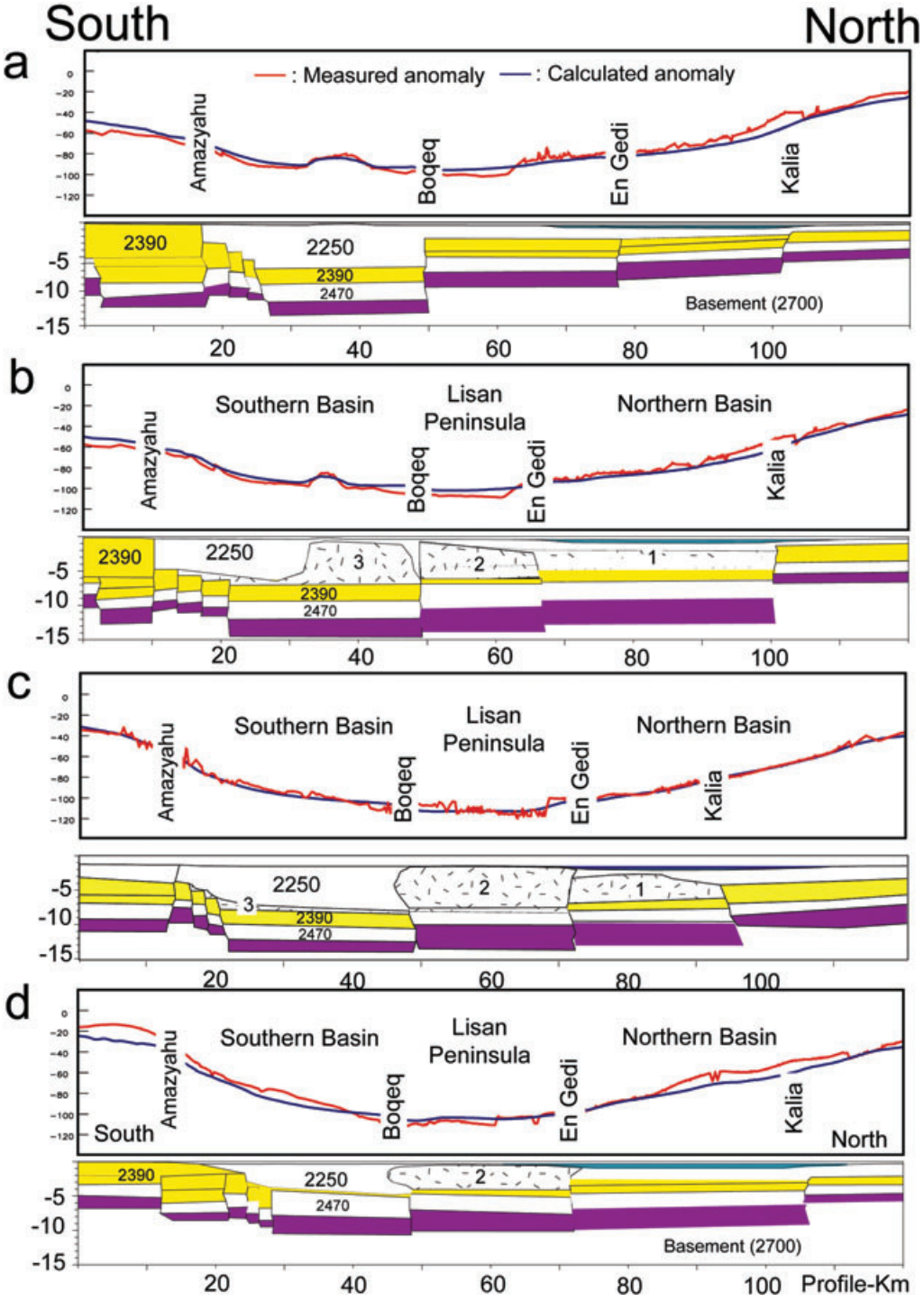

Figure 12. Four vertical N–S sections through the 3-D density model (for location of profiles see Fig. 5). The densities of the geological units are given in kilograms per cubic metre. In the model, three areas of salt diapir are inferred: 1 is located on the western margin of the Dead Sea, 2 is the Lisan salt diapir and 3 is the Sedom salt diapir. The inferred salt diapir labelled '1' extends only from the central part of the Dead Sea to the vicinity of its western bank, with a thickness that decreases from 4 km in the centre (c) to less than 1 km in the west (b). The thickness of the Lisan salt diapir labelled '2' varies from about 8 km in its centre to about 3 km on its western (b) and eastern edges (d). The salt diapir labelled '3' may extend from the southwestern part of the southern Dead Sea subbasin into the southeastern part, with a thickness decreasing from about 6 km to less than 1 km.

(Fig. 5) can provide a satisfying coincidence. The contour map of misfit between the measured and computed Bouguer anomalies (Fig. 13B) reveals an average discrepancy of about $\pm 6.0 \times 10^{-5}$ m s^{-2} (*SD* in Fig. 13C). The discrepancy in the area of the DSB is less than $\pm 4.0 \times 10^{-5}$ m s^{-2}.

The residual gravity field (Fig. 14A) is now compared with the spatial distribution of modelled salt diapir, and the distribution of shallower earthquake events (depth <10 km, magnitude <3.0, Fig. 14B, Hofstetter *et al.* 2000). The largest volume of the salt diapir labelled '2' in Fig. 14B is located beneath the Lisan Peninsula.

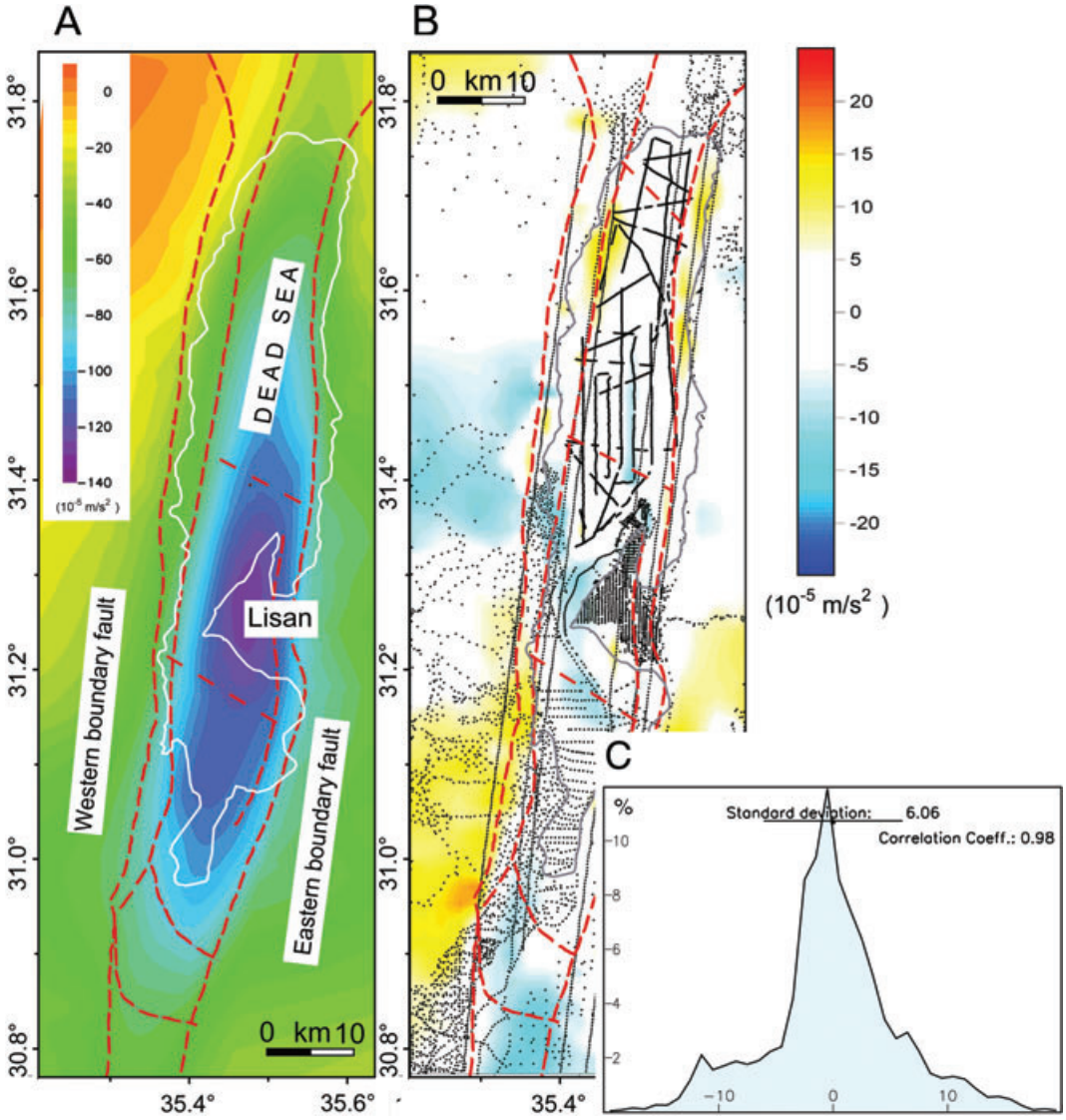

Figure 13. The modelled anomaly (A), the contour map of misfit between the measured (Fig. 5) and the modelled Bouguer anomalies (B) and the histogram of the anomaly difference (C) are shown. The correlation coefficient of 0.98 and standard deviation of about $\pm 6.0 \times 10^{-5}$ m s^{-2} (C) means that the computed gravity anomalies (A) are matching well with the observed anomalies.

Other interpreted salt diapirs are probably located in the western part of the Dead Sea (labelled '1' in Fig. 14B) and in the southwestern part of the southern subbasin (labelled '3' in Fig. 14B). The average depth to the top of the salt diapir ranges from about 2 km beneath the Dead Sea (labelled '1' in Fig. 14B) to 0.5 km beneath the Lisan Peninsula (labelled '2' in Fig. 14B). The short wavelength negative residual anomalies of approximately -30×10^{-5} m s^{-2} (Fig. 14A) are caused by the spatial distribution of salt diapirism within the Pleistocene to Holocene sediment infill. The shallower microearthquake events, which are registered in the vicinity of the modelled salt diapir, might be associated with the movement of salt diapir in the DSB. The volume of the inferred salt segmentation beneath the Dead Sea amounts of about 150 km^3, being some 7 km wide, 7 km long and 3 km thick. In contrast, the areal average dimensions of the Lisan salt diapir, according to our interpretation, are about 10 km by 20 km, with an average thickness of approximately 6 km, giving a volume of approximately 1200 km^3 which is larger than the volume inferred from the 2-D seismic interpretation (about 780 km^3; Al-Zoubi & ten Brink 2001). The Sedom salt diapir (labelled '3' in Fig. 14B) has a volume of about 200 km^3 (being about 5 km wide, 10 km long and 4 km thick), which is also larger than the previously inferred 68 km^3 (Al-Zoubi & ten Brink 2001). These differences in volume are due to the different interpretations of dimensions between 2-D seismic and 3-D gravity methods. The results of gravity interpretation and 3-D density modelling support that the region between the Dead Sea and the Lisan Peninsula (the black box in Fig. 14B) is the deepest part in the DSB, where the tips of the propagating faults met and overlapped with each other as proposed by Mechie *et al.* (2009).

6 CONCLUSIONS

The new compilation of a Bouguer gravity data map, which contains the conventional data set for the entire DSB area, was reinterpreted by (1) 3-D density modelling that incorporated additional information obtained from other geophysical research, (2) regional and residual filtering in the gravity field and (3) curvature analysis and

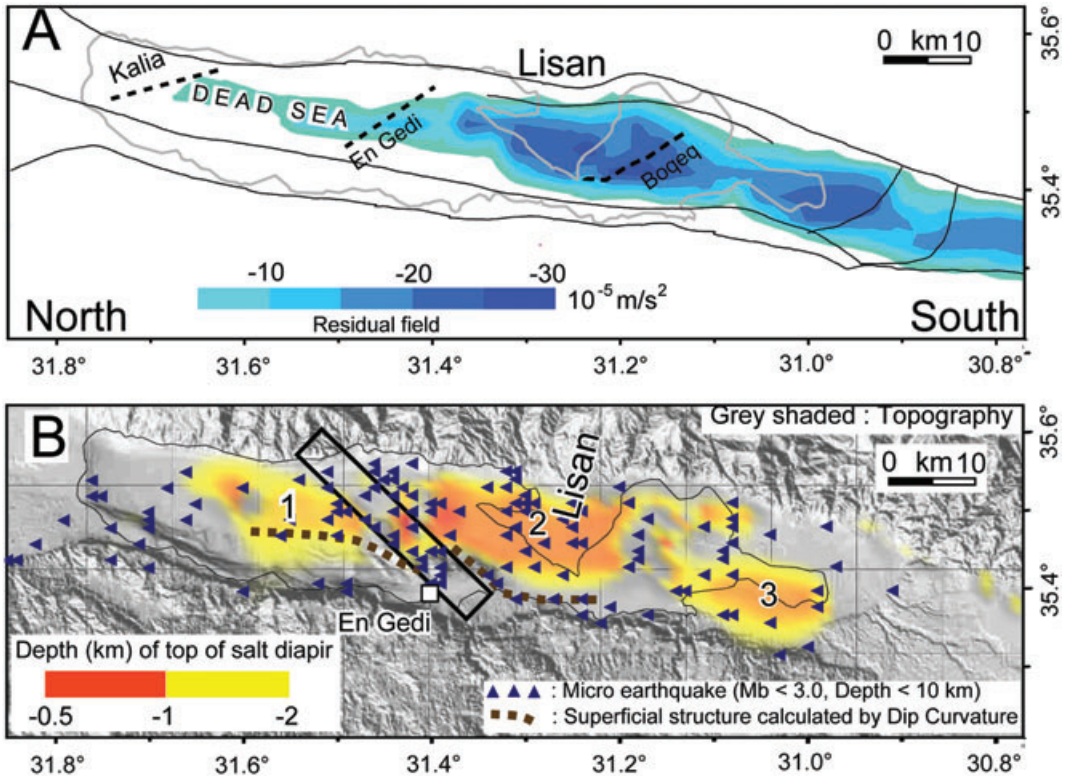

Figure 14. Spatial distribution of the inferred salt diapirs (B) compared to the residual gravity trend (A) and shallower earthquake distribution (blue triangles in B). The largest salt diapir (labelled '2') in the DSB is locating beneath the Lisan Peninsula. The others can be seen in the western part of the Dead Sea (labelled '1') and in the southwestern part of the southern subbasin (labelled '3'). Comparison between shallower earthquake occurrences and the spatial distribution of salt diapirs leads us to infer that these earthquake events are related to the movement of salt diapirism. The black box in B is the deepest part in the DSB, which is resulted by the gravity interpretation and 3-D density modelling.

Euler deconvolution of the gravity field. These methods enabled us to obtain rather detailed information of crustal structures from the southern and to the northern DSB. The seismic interpretation, earthquake data analysis, geometric features assist the 3-D modelling and interpretation of the Bouguer gravity field, revealing aspects of the crustal structures in the DSB that were useful in providing supplementary constraints for the geological and tectonic synthesis. Due to the ambiguity of potential field interpretation, the 3-D density model presented in this paper is probably one of several possible models that have been developed by an iterative, interactive procedure, trying to satisfy as much constraining data as is presently available. The thickness of the sedimentary infill overlying the basement in the DSB decreases from 14 km in the vicinity of the Lisan Peninsula to 8 km in the northern and the southern subbasins. The large negative gravity anomalies (smaller than -100×10^{-5} m s^{-2}) observed over the DSB correspond with the spatial distribution of salt diapir with an average density of 2080 kg m^{-3}. In the vicinity of the western margin of the Dead Sea, a segment of salt diapir with a thickness of about 4 km has been identified at a depth of about 2 km. The shallower microearthquakes registered in the DSB might be associated with the movement of salt diapir in the DSB.

ACKNOWLEDGMENTS

We thank the reviewers Dr. A. Karaki and Dr. D. Closson for their helpful comments; in particular we express our gratitude to Dr. M. Diament whose comments helped to improve the paper substantially. Logistical help was provided by the directors and colleagues of both the GII (Israel) and the NRA (Jordan). Administrational support was given by the Ministry of Defence in Israel, the Jordan Civil Aviation Authority in Amman and the German Embassies in Tel-Aviv and Amman. During the survey, we received help in the field from I. Heyde, S. Hofmann, G. Haim (GII), K. Abbu-Ayash, K. Abu-Hamideh and J. Khataibeh (NRA) and our technicians and pilots. We thank all DESIRE colleagues and M. Rybakov for their ongoing interest, help and advice. The project is financed by the German Research Foundation, which is thankfully acknowledged. This is a publication of the DESIRE Project.

REFERENCES

Aftabi, P., Roustaie, M., Alsop, G.I. & Talbot, C., 2010. InSAR mapping and modelling of an active Iranian salt extrusion, *J. Geol. Soc. Lond.,* **167,** 155–170, doi:10.1144/0016-76492008-165.

Aldersons, F., Ben-Avraham Z., Hofstetter, A., Kissling, E. & Al-Yazjeen, T., 2003. Lower-crustal strength under the Dead Sea Basin from local earthquake data and rheological modelling, *Earth planet. Sci. Lett.,* **214,** 37–59.

Al-Khalidi, K., Aub Ayyash, K., Al-Nabulsi, S. & Sabha, M., 1997. *Petroleum Exploration Opportunities in Jordan*, pp. 63, Natural Resources Authority of Jordan Press, Amman.

Al-Zoubi, A. & Ben-Avraham, Z., 2002. Structure of the earth's crust in Jordan from potential field data, *Tectonophysics*, **346,** 45–59.

Al-Zoubi, A. & ten Brink, U.S., 2001. Salt diapirs in the Dead Sea Basin and their relationship to Quaternary extensional tectonics, *Mar. Pet. Geol.,* **18,** 779–797.

Baer, G., Schattner, U., Wachs, D., Sandwell, D., Shimon, W & Grydman, S., 2002. The lowest place on Earth is subsiding: an InSAR perspective, *Geol.*

Soc. Am. Bull., **114,** 12–23, doi:10.1130/0016-7606(2002)114<0012:TLPOEI>2.0.CO;2.

Ben-Avraham, Z. & Schubert, G., 2006. Deep 'drop down' basin in the southern Dead Sea, *Earth planet. Sci. Lett.,* **251,** 254–263, doi:10.1016/j.epsl.2006.09.008.

Ben-Avraham, Z., Lyakhovsky, V. & Schubert, G., 2010. Drop-down formation of deep basins along the Dead Sea and other strike-slip fault systems, *Geophy. J. Int.,* **181,** 185–197, doi:10.1111/j.1365-246X.2010.04525x.

Closson, D & Abou Karaki, N., 2010. Landslides along the Jordanian Dead Sea coast triggered by the lake level lowering, *Environ. Earth Sci.,* **59**(7), 1417–1430.

Degro, T., 1986. Zur Interpretation gravimetrischer und magnetischer Feldgrößen mit Hilfe von Übertragungsfunktion, *Dissertation*, TU-Clausthal, Clausthal-Zellerfeld.

European Mediterranean Seismological Centre (EMSC), 2004. Earthquake mb 5.1 in Dead Sea region, Jerusalem, http://www.emsc-csem.org/Html/DEADSEA_110204.html (last accessed 2004 February 11).

Fonofoff, N.P. & Millard, R.C., 1983. Algorithms for computation of fundamental properties of sea water, *UNESCO Tech. Pap. Mar. Sci.,* Vol. 44, p. 53, UNESCO, Paris.

Föster, A., Föster, H-J., Masarweh, R., Masri, A., Tarawneh, K. & DESERT Group, 2007. The surface heat flow of the Arabian Shield in Jordan, *J. Asian Earth Sci.,* **30,** 271–284, doi:10.1016/j.jseaes.2006.09.002.

Gardosh, M., Kashai, E., Salhov, S., Shulman, H. & Tannenbaum, E., 1997. Hydrocarbon expliration in the southern Dead Sea area, in *The Dead Sea. The Lake and Its Setting*, p. 286, eds Niemi, T.M., Ben-Avraham, Z. & Gat, J.R., Oxford University Press, New York, NY.

Garfunkel, Z., 1981. Internal structure of the Dead Sea leaky transform (rift) in relation to plate kinematics, *Tectonophysics*, **80,** 81–108.

Garfunkel, Z. & Ben-Avraham, Z., 1996. The structure of the Dead Sea, *Tectonophysics*, **266,** 155–176.

Ginzburg, A. & Ben-Avraham Z., 1997. A seismic refraction study of the northern basin of the Dead Sea, Israel, *Geophys. Res. Lett.,* **24,** 2063–2066.

Götze, H.-J., 1984. Über den Einsatz interaktiver Computergrafik in Rahmen 3 dimensionaler Interpretationstechniken in Gravimetrie und Magnetik Habiltationsschrift. TU Clausthal, p. 236.

Götze, H-J. & Lahmeyer, B., 1988. Application of three-dimensional interactive modeling in gravity magnetics, *Geophysics*, **53**(8), 1096–1108.

Götze, H-J. & Schmidt, S., 2002. Geophysical 3D modeling using GIS-Functions, 8th annual conference of the international association for mathematical geology, *Terra Nostra*, 87–92, ISSN:0946–8978.

Götze, H.-J., El-Kelani, R., Schmidt, S., Rybakov, M., Hassouneh, M., Förster, H.-J., Ebbing, J. & DESERT Group, 2007. Integrated 3D density modelling and segmentation of the Dead Sea Transform (DST), *Int. J. Earth Sci.,* **96,** doi:10.1007/s00531-006-0095-5.

Götze, H.-J., Meyer, U & Choi, S., 2010. *Helicopter Gravity survey in the Dead Sea area*, EOS.

Hall, J.K., 1996. The GSI digital terrain model (DTM) project completed. Israel Geological Survey, *Curr. Res.,* **8,** 47–60.

Hassouneh, M., 2003. Interpretation of potential fields by modern data processing and 3-dimensional gravity modelling of the Dead Sea pull-apart basin/Jordan Rift Valley (JRV), p. 110, *Dissertation*, Uni Würzburg.

Hofstetter, A., Dorbath, C., Rybakov, M. & Goldschmidt, V., 2000. Crustal and upper mantle structure across the Dead Sea rift and Israel from teleseismic P-wave tomography and gravity data, *Tectonophysics*, **327,** 37–59.

Lyngsie, S.B., Thybo, H. & Rasmussen, T.M., 2006. Regional geological and tectonic structures of the North Sea area from potential field modelling, *Tectonophysics*, **413,** 147–170.

Mechie, J., Abu-Ayyash, K., Ben-Avraham, Z., El-Kelani, R., Qabbani, I., Weber, M. & DESIRE Group, 2009. Crustal structure of the southern Dead Sea basin derived from project DESIRE wide-angle seismic data, *Geophys. J.Int.,* **178,** 457–478, doi:10.1111/j.1365-246X.2009.04161.x.

Pašteka, R., Richter, F.P., Karcol, R., Brazda, K. & Hajach, M., 2009. Regularized derivatives of potential fields and their role in semi-automated interpretation methods, *Geophys. Prospect.,* **57,** 507–516, doi:10.1111/j.1365-2478.2008.00780.x.

Petrunin, A.G. & Sobolev, S.V., 2008. Three dimensional numerical models of the evolution of pull-apart basins, *Phys. Earth planet. Inter.,* **171,** 387–399.

Reid, A.B., Allsop, J.M., Granser, H., Millet, A.J. & Somerton, I.W., 1990. Magnetic interpretation in three dimensions using Euler deconvolution, *Geophysics*, **55,** 80–91.

Reilinger, R. *et al*., 2006. GPS constraints on continental deformation in the Africa-Arabia-Eurasia continental collision one and implications for the dynamics of plate interactions, *J. geophys. Res.,* **111,** doi:10.1029/2005JB004051.

Roberts, A., 2001. Curvature attributes and their application to 3D interpreted horizons, *First Break*, **19**(2), 85–99.

Rowan M.G., Jacken, M. & Trudgill, B., 1999. Salt-Related fault families and Fault Welds in the Northern Gulf of Mexico, *AAPG Bull.,* **83**(9), 1454–1484.

Rybakov, M., Goldshmidt, V., Rotstein, Y., Fleischer, L. & Goldberg, I., 1999. Petrophysical constraints on gravity/magnetic interpretation in Israel, *Leading Edge*, **18**(2), 269–272.

Schmidt, S. & Götze, H.-J., 1998. Interactive visualization and modification of 3D models using GIS functions, *Phys. Chem. Earth*, **23**(3), 289–295.

Schmidt, S. & Götze, H.-J., 2003. Pre-interpretation of potential fields by the aid of curvature attributes, *Geophys. Res., Abstr.,* **6**, 07689.

Schmidt, S., Götze, H.-J., Siehl, A. & Tasárová, Z., 2004. 3D Gravity and Magnetic Modelling and Integration of Constraints Using Open GIS: The IGMAS Software Package, in *Proceedings of the ASEG 17th Geophysical Conference and Exhibition*, Sydney.

Schmidt, S., Götze, H.-J., Fichler, Ch. & Alvers, M., 2010. IGMAS+ a new 3D Gravity and Magnetic Modeling Software, in *Die Welt im Netz*, pp. S57–63, eds Zipf, A., Behncke, K., Hillen, F. & Schefermeyer, J., Akademiesche Verlagsgesellschaft AKA GmbH, Osnabrück, Germany. ISBN 978–3-89838–335-6.

Shimoni, M., Hanssen, R.F., Van Der Meer, F., Kampes, B.M. & Ben Dor, E., 2002. Salt diapir Movements using SAR interferometry in the Lisan peninsula, Dead Sea Rift, *Proc. SPIE,* **4543,** 151–160.

Sobolev, S.V. & Babeyko, AYU, 1994. Modelling of mineralogical cimposition, density and elastic wave velocities in anhydrous magmatic rocks, *Surv. Geophys.,* **15,** 515–544.

Ten Brink, U.S., Ben;Avraham, Z., Bell, R.E., Hassouneh, M., Coleman, D.F., Andreasen, G., Tibor, G. & Coakley, B., 1993. Structure of the Dead Sea pull;apart basin from gravity analysis, *J. geophys. Res.,* **98,** 21877–21894.

Thomson, D.T., 1982. EULDPH: a new technique for making computer-assisted depth estimates from magnetic data, *Geophysics*, **47,** 31–37.

Weber, M. & DESERT group, 2009. Anatomy of the Dead Sea Transform from lithospheric to microscopic scale, *Rev. Geophys.,* **47,** RG2002, doi:10.1029/2008RG000264.

Yechieli, Y., Abelson, M., Bein, A., Crouvi, O. & Shtivelman, V., 2006. Sinkhole "swarms" along the Dead Sea coast: reflection of disturbance of lake and adjacent groundwater systems, *Geol. Soc. Am.,* **118**(9/10), 1075–1087, doi:10.1130/B25880.1.